



Hybridization of rutile TiO₂ (rTiO₂) with g-C₃N₄ quantum dots (CN QDs): An efficient visible-light-driven Z-scheme hybridized photocatalyst



Yuhan Li ^a, Kangle Lv ^{a,b,*}, Wingkei Ho ^{a,*}, Fan Dong ^c, Xiaofeng Wu ^b, Yang Xia ^b

^a Department of Science and Environmental Studies, The Education University of Hong Kong, Tai Po, N.T., Hong Kong, PR China

^b Key Laboratory of Catalysis and Materials Science of the State Ethnic Affairs Commission and Ministry of Education, College of Resources and Environmental Science, South-Central University for Nationalities, Wuhan, 430074, PR China

^c Chongqing Key Laboratory of Catalysis and Functional Organic Molecules, College of Environmental and Biological Engineering, Chongqing Technology and Business University, Chongqing, 400067, PR China

ARTICLE INFO

Article history:

Received 27 June 2016

Received in revised form

18 September 2016

Accepted 24 September 2016

Available online 26 September 2016

Keywords:

g-C₃N₄

Rutile TiO₂

Quantum dots

Photocatalytic degradation

Visible-light

ABSTRACT

To make full use of solar light, fabrication of g-C₃N₄ quantum dots (CN QDs) modified rutile TiO₂ (rTiO₂) hybrid (CN QDs-rTiO₂), using both visible light responsive semiconductors as components, was successfully achieved by calcination the mixture of P25 TiO₂ and melamine at 500 °C for 4 h. It was found that CN QDs were *in-situ* formed during calcination, which were homogeneously deposited on the surface of rTiO₂. Modification of rTiO₂ by CN QDs not only improved the visible-light harvesting ability, but also retarded the recombination of photo-generated electron-hole pairs. CN QDs-rTiO₂ hybrid (S15) with nominal 15 at.% CN QDs loading showed the highest photocatalytic activity among all the photocatalysts, whatever for degradation of RhB or photocatalytic decomposition of NO, under visible light irradiation. The increased formation of •OH radicals in CN QDs modified rTiO₂ suspensions supports a Z-Scheme degradation mechanism instead of the formation of CN QDs-rTiO₂ heterojunctions.

© 2016 Elsevier B.V. All rights reserved.

1. Introduction

The increasing world crises of clean energy supply and the expanding environmental pollution have become crucial issues in the past few years. It is of significant importance to develop various effective strategies and solutions to resolve these problems [1,2]. The outstanding performance of photocatalysis pioneered by Fujishima et al. make it available in diverse application fields, which has been regarded as one of the most promising technology because of its considerable potential in alleviating, and even solving both the current energy crisis and environmental deterioration [3]. To date, various types of photocatalytic materials have been developed [4–8]. Since the first report on photocatalytic splitting of water on TiO₂ electrodes was published in 1972, TiO₂ as photocatalyst with chemical stability, non-toxicity, and low cost has demonstrated wide-ranging potential applications in a variety

of areas, such as energy conversion and contaminant degradation, solar cells, and so on [9–14]. However, anatase TiO₂ notoriously suffers from low utilization of solar energy (can only be excited by UV light), resulting in inferior photocatalytic activity, thereby limiting its promising applications in photocatalysis. In addition to the urgent demand for exploring a robust visible-light-responsive photocatalyst, the development of innovative strategies to improve the photocatalytic activity of known potential photocatalysts also performs an indispensable function in developing technologies. Although rutile TiO₂ (rTiO₂) [15] shows poor photocatalytic activity due to its rapid recombination rate of photo-generated electron-hole pairs, it possesses relatively narrow bandgap of 3.0 eV at room temperature, which allows for absorption of visible light and thus undistinguished visible-light-induced photocatalytic activity. Therefore, developing visible-light-driven photocatalysts with superior photocatalytic activity remains a considerable challenge.

Graphite-C₃N₄ (CN) possesses an indirect, narrow bandgap of 2.7 eV, which is known as an attractive promising candidate for visible-light-driven photocatalyst owing to its exceptional photochemical stability and high photocatalytic efficiency [16,17]. However, the photocatalytic performance of CN is poor due to the

* Corresponding authors.

E-mail addresses: lvkangle@mail.scuec.edu.cn (K. Lv), [\(W. Ho\).](mailto:keithho@ied.edu.hk)

low specific surface area, which results in limited numbers of active sites, and rapid recombination of photo-generated electron-hole pairs. Therefore, enhancing the photocatalytic efficiency of C_3N_4 keeps a challenge to date [17,18].

One of the most efficient approaches to improve the photocatalytic performance of semiconductor photocatalyst is through reducing electron-hole recombination via coupling with other semiconductors [19,20]. For example, Zang et al. synthesized a visible-light-driven photocatalyst of brookite TiO_2/CN hybrid, which shows improved photocatalytic activity for As^{3+} oxidation, MO degradation, and hydrogen production [21]. Miranda et al. prepared TiO_2/CN composites with enhanced photocatalytic activity for the degradation of phenol under UV irradiation by a simple impregnation method [22]. Recently, Yu et al. reported a direct $\text{CN}-\text{TiO}_2$ semiconductor-semiconductor Z-scheme heterojunction without an electron mediator by utilization of simple mixed the feedstocks (P25 TiO_2 and urea) calcination strategy, such an extraordinary Z-scheme heterojunction not only elevates charges separation efficiency but also enhances the redox ability by retaining a highly negative CB edge and a highly positive VB edge for better photocatalytic performance [23]. Similarly, Huang et al. also reported the Z-scheme heterojunction between g-CN and TiO_2 hollow nanobox with exposed reactive facets by a facile one-pot solvothermal method [24].

As an attractive candidate for visible light-driven photocatalysis, g- C_3N_4 quantum dots (CN QDs) [25] with excellent optical properties can convert NIR light to visible light and thus promote solar energy harvesting. The ability of employing NIR region light has been used to design CN QDs-based photocatalysts, such as CN QDs- TiO_2 . Currently, Li et al. fabricated CN QDs modified single-crystalline TiO_2 nanotube with high photocatalytic activity in synergistic H_2 production and organic pollutant degradation by an *in-situ* grafting approach [26]; An et al. reported that the photocatalytic performance of CN QDs decorated TiO_2 nanowire arrays was significantly enhanced due to the quantum and sensitization effects of CN QDs [27].

Although there are many papers reported the modification of TiO_2 with CN, all these studies are related to bulk CN and anatase phase TiO_2 [28–31]. The effect of CN QDs modification on the structure and photocatalytic activity of rutile TiO_2 (rTiO_2) has not been reported yet. Since both CN and rTiO_2 are visible-light responsive photocatalysts, it is reasonable to propose that CN/r TiO_2 hybrids possess excellent visible-light harvesting ability, which is of great importance from the viewpoint of practical applications. Please note that the bandgap of anatase and rutile TiO_2 are 3.2 and 3.0 eV, respectively. According to the energy distribution of sunlight spectrum, anatase TiO_2 ($\lambda_{\text{ex}} < 388 \text{ nm}$) can only harvest about 5% of the sunlight, while 11% of the sunlight can be absorbed by rutile TiO_2 ($\lambda_{\text{ex}} < 413 \text{ nm}$).

In the present study, we developed a one-pot strategy to prepare CN QDs/r TiO_2 hybrids. This strategy aims not only to address the drawbacks of anatase TiO_2 with low visible-light-driven photocatalytic activity but also to reduce charge carrier recombination rate by semiconductor coupling. For the first time, the effect of nominal molar ratios of CN QDs to r TiO_2 of 0.05:1, 0.15:1, and 0.25:1, on the structure and photocatalytic activity of QDs-r TiO_2 composite was systematically studied. For simplicity, the hybrids were named as S5, S15, and S25, respectively. Pure r TiO_2 and CN were also used for comparison. Please note r TiO_2 was obtained by directly calcination of P25 TiO_2 at 500 °C for 4 h (see text below). The photocatalytic activity of QDs-r TiO_2 hybrid was evaluated by both degradation of Rhodamine (RhB) and NO oxidation. The mechanism for the enhanced photocatalytic activity of QDs-r TiO_2 hybrid was also discussed.

2. Experimental

2.1. Preparation

Typically, 2.0 g of P25 TiO_2 (Acros Chemical Reagent Corp.) and a certain amount of melamine (Sigma Chemical Reagent Corp.) were mixed in an agate mortar in different molar ratios of 5%, 15%, and 25%, respectively. After being ground for 10 min, the mixtures were placed into an alumina crucible with cover and heated in a muffle furnace at 500 °C for 4 h with a heating rate of 2.3 °C min⁻¹. After air-cooling to room temperature, the resulting powders were collected. The prepared samples are denoted as S5, S15, and S25, respectively. Pure TiO_2 and CN were synthesized by directly heating 2.0 g of P25 TiO_2 and 2.0 g of melamine under the same thermal conditions.

2.2. Characterization

The phase structures of the samples were investigated by using an X-ray diffractometer (XRD; D/max RA, Japan). The morphological characteristics and microstructures of the samples were characterized using scanning electron microscopy (SEM; JEOL JSM-6490, Japan) and transmission electron microscopy (TEM; JEM-2010, Japan). Nitrogen adsorption-desorption isotherms were obtained in a nitrogen adsorption apparatus (ASAP 2020, USA). All of the samples were degassed at 150 °C prior to the measurements to investigate the surface areas and pore size distribution of the samples. Nitrogen adsorption-desorption isotherms were obtained using a nitrogen adsorption apparatus (Micromeritics ASAP 2020, USA) with all samples degassed at 150 °C prior to measurements. The optical properties of samples were obtained in a UV-vis spectrophotometer (UV-vis DRS; UV-2450, Shimadzu, Japan) scan equipped with an integrating sphere assembly. BaSO_4 was used as the reflectance sample. The photoluminescence spectra (PL) of samples were obtained using a fluorescence spectrophotometer (FS-2500, Japan) equipped with a Xe lamp with an optical filter as excitation source to investigate the recombination and separation of photo-generated electrons and holes in the samples. Fourier transform infrared (FT-IR) spectra were recorded by NEXUIS-470 infrared spectrometer (Nicolet Co., USA) using KBr as reference.

The photocurrent measurement of photocatalysts were conducted in a three electrode system using a CHI 760E electrochemical workstation. The photocatalysts were used as working electrode, Pt wire and Ag/AgCl were used as counter electrode and reference electrode, respectively. 0.5 M Na_2SO_4 aqueous solution was used as electrolyte solution. A 3 W LED lamp emitted mainly at 420 nm was used as the light source. The working electrode was prepared by doctor-blade method using ITO glass (1 cm × 1 cm) as substrate. The spreading slurries of sample were prepared by grinding 50 mg of photocatalyst, 30 mg of polyethylene glycol (MW: 20,000) and 800 μl of water. The film was annealed at 250 °C for 30 min after dried in air. Electrochemical impedance studies of photocatalysts was carried out at the open-circuit potential. An ac disturbance of 5 mV was applied to the working electrode on the frequency from 0.1 Hz to 1000 Hz.

Electron spin resonance (ESR) signals of radicals spin-trapped by 5,5-dimethyl-1-pyrroline N-oxide (DMPO) were recorded on a JES FA200 spectrometer. Samples for ESR measurement were prepared by mixing the samples in a 40 mM DMPO solution tank (aqueous dispersion for DMPO-OH^\bullet and methanol dispersion for $\text{DMPO-O}_2^{\bullet-}$) and irradiated with visible light ($\lambda > 420 \text{ nm}$).

2.3. Evaluation of the photocatalytic activity

Photocatalytic activity of as-prepared samples for degradation of aqueous RhB was evaluated in a quartz glass reactor. A 0.05 g

portion of as-synthesized sample was dispersed in RhB aqueous solution (50 mL, 5 mg L⁻¹). The light irradiation system includes a 500 W Xenon lamp with a jacket of flowing water to eliminate the temperature effect. Before irradiation, the suspension was allowed to reach equilibrium with continuous stirring for 60 min.

The degradation efficiency of RhB was evaluated using the UV-vis absorption spectra (Hitachi U-3310) to measure the peak value of a maximum absorption of RhB solution. During irradiation, 3.0 mL of suspension was periodically taken from the reaction cell at given time intervals (60 min) for subsequent dye concentration analysis after centrifugation (9000 rpm, 5 min). The maximum absorption of RhB is at wavelength of 554 nm. The removal ratio (%) can be calculated as $\eta (\%) = (C_0 - C)/C_0 \times 100\%$, where C_0 is the initial concentration of RhB and C is the revised concentration after irradiation.

Triethanolamine (TEA), *tert*-butyl alcohol (TBA), and N₂ gas flow were selected as scavengers of photo-generated holes, hydroxide radical (•OH), and O₂•⁻, respectively. Before light irradiation, 0.05 g of photocatalyst and 0.1 mL of TEA or 0.1 mL of TBA or N₂ gas flow was added into 50 mL of RhB solution (5 mg L⁻¹), and the suspensions were magnetically stirred in the dark for 1 h to reach sorption equilibrium. Furthermore, all experiments were performed at room temperature under constant stirring. Every interval of 1 h, 3.0 mL of suspension was collected and analyzed using a UV-vis spectrophotometer.

The photocatalytic activity of the as-prepared CN QDs-TiO₂ composites were also evaluated in terms of the oxidation of NO at ppb levels in a continuous flow reactor at 25 °C. The volume of the rectangular reactor composed of stainless steel and covered with quartz glass was 4.5 L (30 cm × 15 cm × 10 cm; $L \times W \times H$). A visible light LED lamp was used as a simulated visible light source. Afterward, 0.2 g of the as-prepared photocatalyst was added into 30 mL of H₂O and ultrasonicated for 30 min. The resulting suspension was coated onto a dish with a diameter of 11.5 cm. The coated dish was pretreated at 70 °C to evaporate water thoroughly and then cooled to room temperature prior to photocatalytic testing. NO gas was acquired from a compressed gas cylinder containing 50 ppm of NO (N₂ balance) in accordance with traceable standards recommended by the National Institute of Standards and Technology. The initial NO concentration was diluted to approximately 600 ppb by an air stream supplied by a zero-air generator (A Teledyne Technol. Co., Model 701). The gas streams were completely premixed in a gas blower, and the flow rate was controlled with a mass flow controller at 1.0 L min⁻¹. After adsorption-desorption equilibrium was achieved, the lamp was turned on. NO concentration was continuously measured by using a chemiluminescence NO_x analyzer (A Teledyne Technol. Co., Model T200), which monitors NO, NO₂, and NO_x (NO_x represents NO + NO₂), at a sampling rate of 1.0 L min⁻¹.

3. Results and discussion

3.1. Phase structure

Fig. 1 shows the X-ray diffraction (XRD) information regarding the phase and crystalline composition of these CN QDs-TiO₂ samples, as well as the pure CN and TiO₂ samples. The diffraction peaks of CN are correlated closely with the documented graphite-like hexagonal phase of g-C₃N₄ (JCPDS, Card No. 87-1526), with two pronounced peaks at 2θ values of 13.0° and 27.5° are assigned to (100) and (002) crystal planes for the graphitic material [32,33], respectively. As for the pure TiO₂ sample, the peaks can be indexed to the dominant rutile phase (JCPDS no. 21-1276) with minor anatase phase (JCPDS no. 21-1272), implying the phase transformation of P25 TiO₂ from anatase to rutile due to calcination. According to Scherrer equation [34], the weight content of rutile phase in

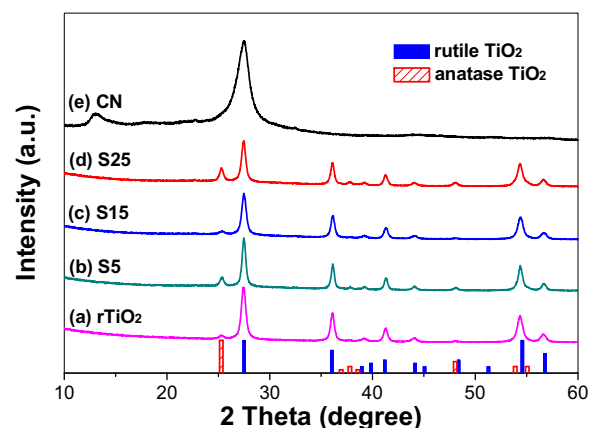


Fig. 1. XRD patterns the photocatalysts, together with the expected diffraction peaks for anatase and rutile TiO₂, respectively.

TiO₂ for S15 sample is only about 6%. Therefore, we can simply denote the calcined P25 TiO₂ as rTiO₂ (rutile TiO₂). For CN QDs-rTiO₂ composites, the peaks match well with the standard XRD patterns of rutile TiO₂, and no different diffraction peaks for g-C₃N₄ can be observed in the CN QDs-rTiO₂ hybrids. This finding can be attributed to the fact that the weight-loading of CN QDs was extremely low, which were well-dispersed on the surface of rTiO₂, and the diffraction peaks related to CN could be overlapped by the diffraction peaks of rTiO₂. Moreover, the XRD patterns of CN QDs-rTiO₂ hybrids with different molar ratios of CN QDs do not differ from that of rTiO₂. Therefore, modification with CN QDs shows little effect on the phase structure of rTiO₂, which is advantageous for the photocatalytic properties of the as-prepared nanocomposites [35].

3.2. Morphology and microstructure

Fig. 2 displays the SEM images of S15 composite, together with pure CN and rTiO₂ samples. From **Fig. 2a**, we can see an aggregated, chunky and lamellar structured CN, which is in size of several micrometers. **Fig. 2b** exhibits the rough surface of rTiO₂ microspheres in diameters of approximately 2–3 μm, which come from the assembly of rTiO₂ nanoparticles. As shown in **Fig. 2c** and d, after the introduction of 15% molar ratio of CN QDs, some tiny particles are deposited on the surface of rTiO₂, forming a heterostructure and thereby demonstrating successful grafting of CN QDs onto rTiO₂. In addition, no remarkable change in particle size and morphology can be observed, thus confirming that CN QDs materials are not incorporated into the lattice of rTiO₂. This result is in accordance with XRD patterns.

The microstructure and morphology of the as-synthesized samples were further investigated by TEM. As shown in **Fig. 3a** and b, CN presents a bulk layer structure, whereas the rTiO₂ shows two characteristic lattice fringes with separated distances of 2.4 and 3.5 Å, corresponding to the (001) crystalline face of the rutile phase TiO₂ [36] and the (101) crystalline face of the anatase phase TiO₂ [37], respectively. Upon the introduction of CN QDs, no change in lattice structure of rTiO₂ and CN QDs was observed as shown in **Fig. 3c**. There are many dark dots homogeneously deposited on the surface of TiO₂ nanoparticles, which should be CN QDs (TEM images of Fig. S1). From the HRTEM images of **Fig. 3c** and d, an extremely close interface between the CN QDs and rTiO₂ was found in the composite to form heterojunctions. Thus, this fact suggests that the annealing process is necessary for the integrated composite, and the hybrid possesses a heterostructure rather than a physical mixture of two separate phases of CN QDs and rTiO₂. This form is beneficial for superior photocatalytic performance. Furthermore, as can be seen from **Fig. 3d**, typical TEM image shows that CN QDs are in average

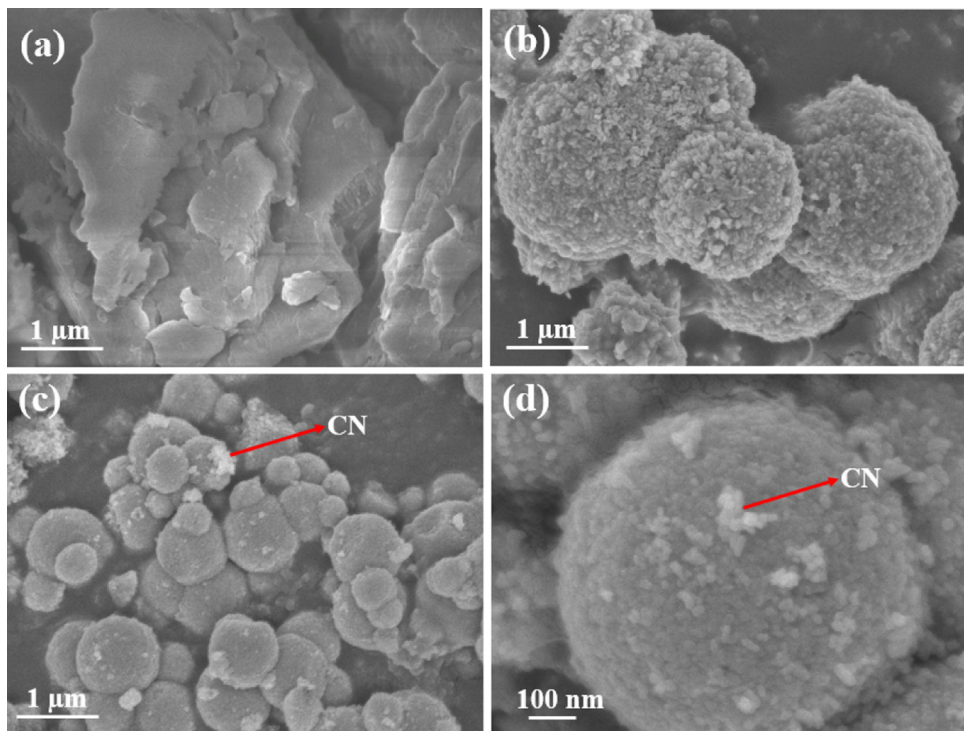


Fig. 2. SEM images of bulk $\text{g-C}_3\text{N}_4$ (a), rTiO_2 (b) and S15 sample (c and d). The red arrows indicate the presence of CN QDs (For interpretation of the references to colour in this figure legend, the reader is referred to the web version of this article.)

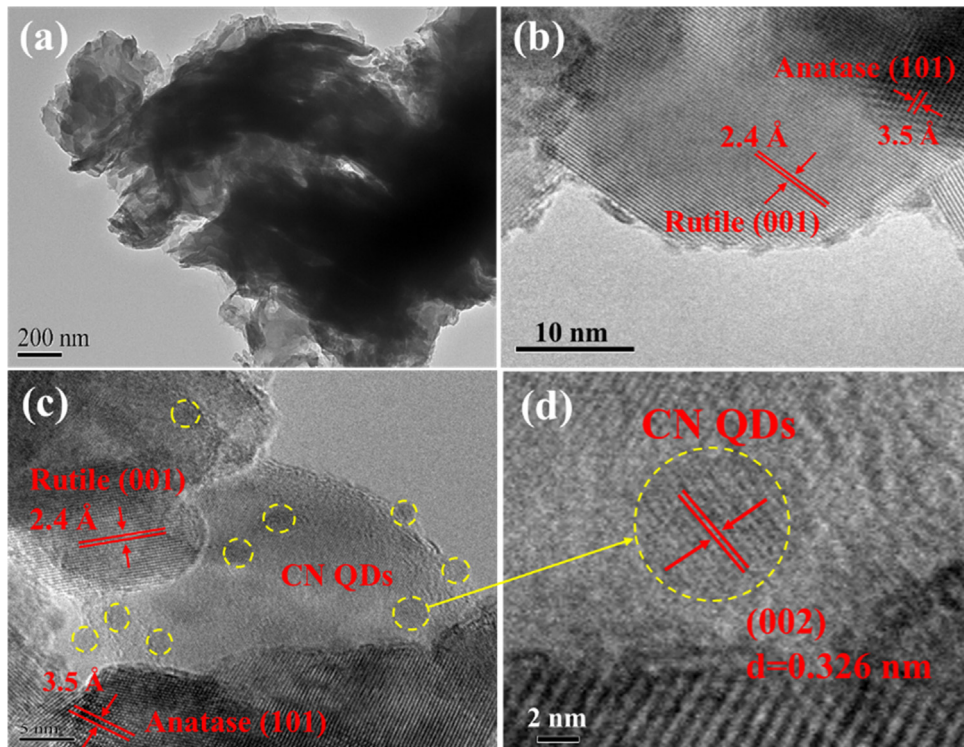


Fig. 3. TEM image of bulk $\text{g-C}_3\text{N}_4$ (a), HR TEM images of rTiO_2 (b), S15 sample (c) and CN QDs (d). The yellow circles represent the presence of CN QDs (For interpretation of the references to colour in this figure legend, the reader is referred to the web version of this article.)

diameter of around 4 nm with a lattice spacing of 0.326 nm, corresponding to the (002) plane of hexagonal $\text{g-C}_3\text{N}_4$ (JCPDS 87-1526) [38]. Based on these experimental results, it can be proposed that

TiO_2 nanoparticles prevent the polymerization of melamine to produce bulk $\text{g-C}_3\text{N}_4$. Instead, smaller $\text{g-C}_3\text{N}_4$ particles (CN QDs) was in-situ formed on the surface of rTiO_2 .

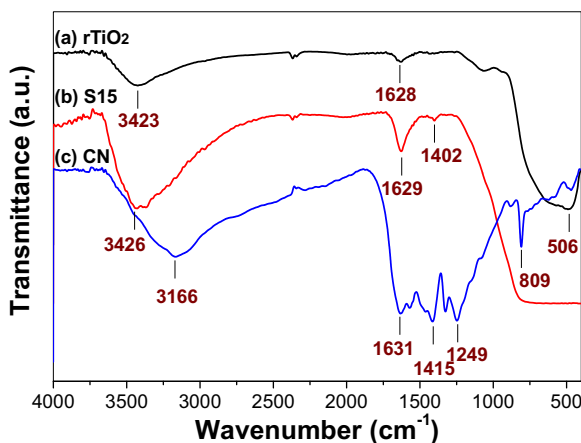


Fig. 4. Comparison of the FT-IR spectra of rTiO₂ (a), CN QDs modified rTiO₂ (b) and g-C₃N₄ sample (c), respectively.

3.3. FT-IR spectra

FT-IR spectrum was used to further study the structure of CN QDs modified rTiO₂ hybrid. For pure rTiO₂, three main absorption regions can be clearly observed (Fig. 4a). The broadband peak centered at 3423 cm⁻¹ is attributed to the O-H stretching of physisorbed water on the surface of TiO₂, and the relatively sharp band at 1628 cm⁻¹ corresponds to the O-H bending modes of water molecules. The strong absorption observed below 850 cm⁻¹ could be attributed to the absorption of Ti-O-Ti [24]. Three main absorption regions were observed for bulk g-C₃N₄ (Fig. 4c), where the broad peak centered at 3166 cm⁻¹ is ascribed to the stretching vibration of N-H, and several typically strong bands in the range of 1249–1631 cm⁻¹ are attributed to the typical stretching vibration of C-N heterocycles, and the peak at 809 cm⁻¹ can correspond to the breathing mode of triazine units [19].

Fig. 4b shows the FT-IR spectrum of CN QDs modified rTiO₂, using S15 as an example. It can be seen that the spectrum of S15 is similar to that of rTiO₂ (compare Fig. 4a and b), excepts the formation of a new peak centered at 1402 cm⁻¹, which was attributed to the typical stretching vibration of C-N heterocycles, conforming the formation of g-C₃N₄ in hybridized S15 sample. When compared with the FT-IR spectrum of bulk g-C₃N₄ (Fig. 4c), this peak shifted from 1415 cm⁻¹ to 1402 cm⁻¹, also reflecting the strong reaction between CN QDs and rTiO₂, which is consistent with the characterization results of TEM (Fig. 3 and Fig. S1). This strong interfacial interaction between CN QDs and rTiO₂ would facilitate the electron transfer, and therefore improve the photocatalytic efficiency.

3.4. Optical property

The optical properties of CN QDs-rTiO₂ composites, pure CN, and rTiO₂ samples were examined using the DRS technique, and the results are shown in Fig. 5A. The pristine rTiO₂ shows its fundamental absorption edge rising at around 420 nm, which can be assigned to the intrinsic band gap of 3.0 eV [39]. The absorption onset of CN is about 520 nm, thus enabling rTiO₂ to be sensitized and extending the optical response. The absorption spectrum of g-C₃N₄ is closely related to the precursor and calcination temperature [40].

We can clearly observe for the series of CN QDs-rTiO₂ hybrids that the absorption intensity in the range of 420–550 nm is significantly enhanced by the introduction of different molar ratios of CN QDs, which enables the hybrids to utilize a higher fraction of the visible-light region. Integrating CN QDs onto rTiO₂ results in considerable red-shift in the absorption onset of rTiO₂, which is implicit

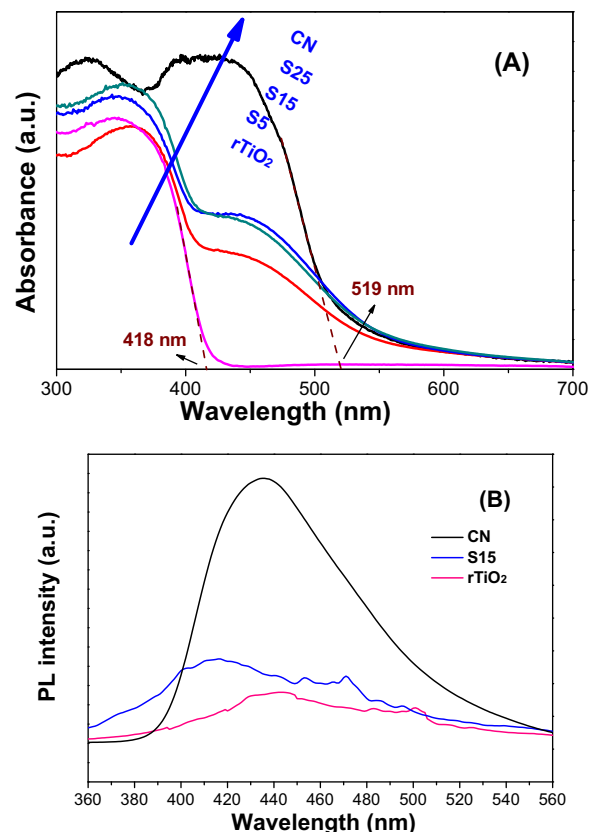


Fig. 5. UV-vis DRS (A) and PL spectra (B) of the photocatalysts.

of the interfacial interaction between CN QDs and rTiO₂. However, CN QDs loading shows an optimum content because excess CN QDs would exert a light screening effect on rTiO₂ microspheres by decreasing the multiple reflection of light from interstitial regions of rTiO₂ nanoparticles [41]. This effect could not allow light to reach the surface of the CN QDs-rTiO₂. These results reveal that the fabrication of the CN QDs-rTiO₂ heterostructure provides considerable potential for modulating the desired optical absorption of photocatalysts and therefore benefits the photocatalytic performance.

PL spectra were obtained (Fig. 5B) to disclose the migration, transfer, and recombination processes of the photogenerated electron-hole pairs in semiconductors. Notably, bare CN exhibits a strong, wide peak in the PL spectrum excited at about 430 nm. However, the PL spectrum characteristics of the CN QDs-rTiO₂ hybrids were similar to those of pure rTiO₂ and markedly weaker than those of CN. An evident PL peak decrease can be observed after the introduction of different molar ratios of CN QDs. This decrease in PL intensity indicates the low recombination rate of photogenerated electrons and holes, as well as a favorable contact between CN QDs and rTiO₂. That is, both improved visible-light harvesting ability and the faster separation of photogenerated charges contribute to enhanced photocatalytic activity.

3.5. Photocurrent and electrochemical impedance study

Photocurrent measurements were carried out for rTiO₂, S15 and CN samples after deposition on ITO electrodes (Fig. 6A). A fast and uniform photocurrent response was observed for each switch-on and switch-off event in all the electrodes. This photoresponsive phenomenon was entirely reversible. It can be seen that the photocurrent of the CN electrode was the lowest (about 0.3 μA) due to the quick recombination of photo-generated electron-hole pairs. The photocurrent of rTiO₂ electrode was 6 times higher than

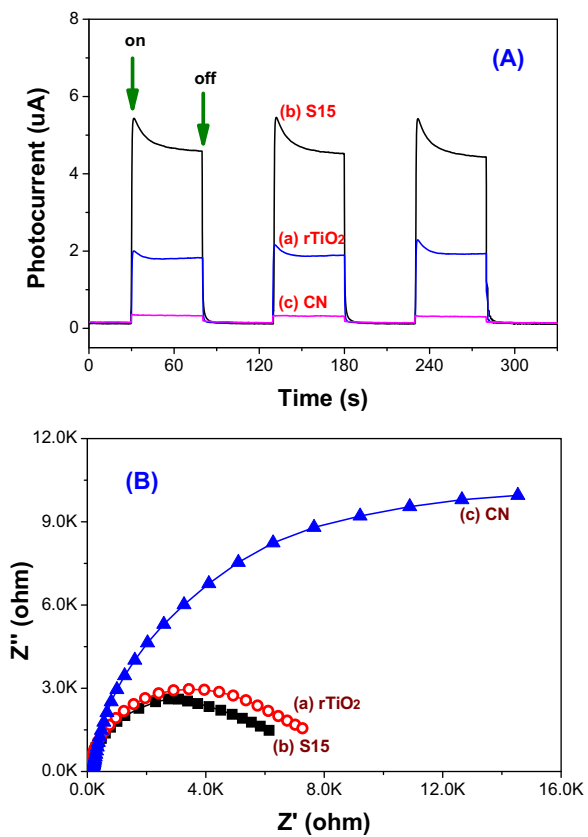


Fig. 6. Comparison of the photoelectrochemical responses (A) and electrochemical impedance spectroscopy (EIS) Nynquist plots (B) for rTiO₂ (a), S15 (b) and CN (c) sample, respectively.

that of CN electrode (about 1.8 uA). However, the photocurrent of CN QDs modified electrode was measured to be as high as about 5.0 uA, which was about 3 times as high as that of the rTiO₂ electrode, indicating that the separation efficiency of photoinduced electrons and holes was improved through the electronic interaction between CN QDs and TiO₂ [42]. The enhanced photocurrent due to CN QDs modification has also been confirmed by surface photovoltage spectroscopy (SPS) shown in Fig. S3.

Fig. 6B compares the electrochemical impedance spectroscopy (EIS) Nynquist plots for pristine CN, TiO₂ and CN QDs modified TiO₂ (S15) electrodes. It can be seen that the diameter of the arc radius on the EIS Nynquist plot of the hybridized S15 electrode is the smallest. The smaller the arc radius of an EIS Nynquist plot means the higher the efficiency of charge separation. Therefore, after modification of rTiO₂ with CN QDs, the photoinduced electrons and holes are separated more efficiently through an interfacial interaction between CN QDs and rTiO₂ [43].

3.6. Nitrogen sorption

The specific surface area of the photocatalyst is considered to be a vital factor that influences the photocatalytic activity. In most cases, a larger surface area could provide more adsorption and/or reactivate sites for photocatalysis, which renders faster migration of charge carriers, resulting in the improvement of photocatalytic reaction rate. For determining the surface area of the as-synthesized samples, N₂ adsorption-desorption isotherms were measured (Fig. 7A) and used to calculate the corresponding pore size distributions (Fig. 7B). The corresponding structural parameters obtained from the adsorption isotherms are summarized in Table 1.

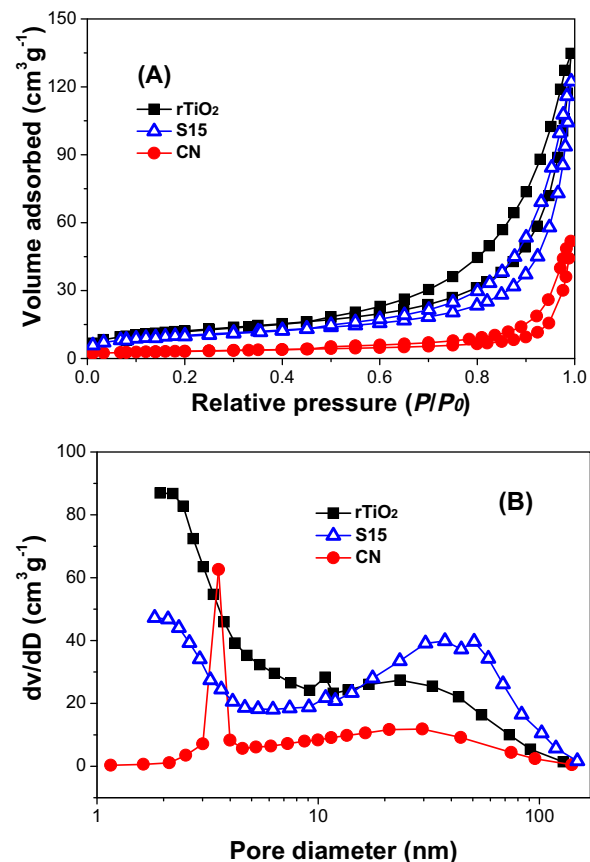


Fig. 7. Nitrogen adsorption-desorption isotherms (a) and the corresponding pore size distribution curves (b) of CN, rTiO₂, and CN QDs-rTiO₂ composite, respectively.

Table 1
Physical properties of the photocatalysts.

Sample	component	S _{BET} (m ² g ⁻¹)	V _{pore} (cm ³ g ⁻¹)	Pore size (nm)
rTiO ₂	rutile TiO ₂	53.3	0.19	2.1/23.6
S5	5% CN QDs-rTiO ₂	45.3	0.30	1.9/36.5
S15	15% CN QDs-rTiO ₂	43.9	0.36	1.8/50.5
S25	25% CN QDs-rTiO ₂	40.2	0.28	2.1/37.6
CN	g-C ₃ N ₄	10.9	0.08	3.6/29.5

As we can see from Table 1, the BET surface area of approximately 10.9, 53.3, 45.3, 43.9, and 40.2 m² g⁻¹ for the CN, rTiO₂, S5, S15, and S25 hybrids, respectively. After the incorporation of CN QDs, the specific surface areas of the CN QDs-rTiO₂ composites decreased with the increase in CN QDs content because of the generation of CN QDs with relatively low specific surface areas; thus, the CN QDs embedded in the interstitial regions of rTiO₂ nanoparticles.

The corresponding pore volume (Fig. 7B) increases from 0.08 cm³ g⁻¹ for CN and 0.19 cm³ g⁻¹ for rTiO₂ to 0.30 cm³ g⁻¹ for S5, 0.36 cm³ g⁻¹ for S15, and 0.28 cm³ g⁻¹ for S25. The increase in pore volume after the introduction of 5% CN QDs and 15% CN QDs can be attributed to the effect of discharged gases from the thermal polycondensation of melamine. However, the decrease in pore volume after the introduction of 25% CN QDs can be ascribed to the excess CN QDs coverage on the rTiO₂ surface and occupying the pores of rTiO₂ microspheres. These results indicate that the improved photocatalytic performance did not result from the change in the specific surface areas of the as-obtained photocatalysts.

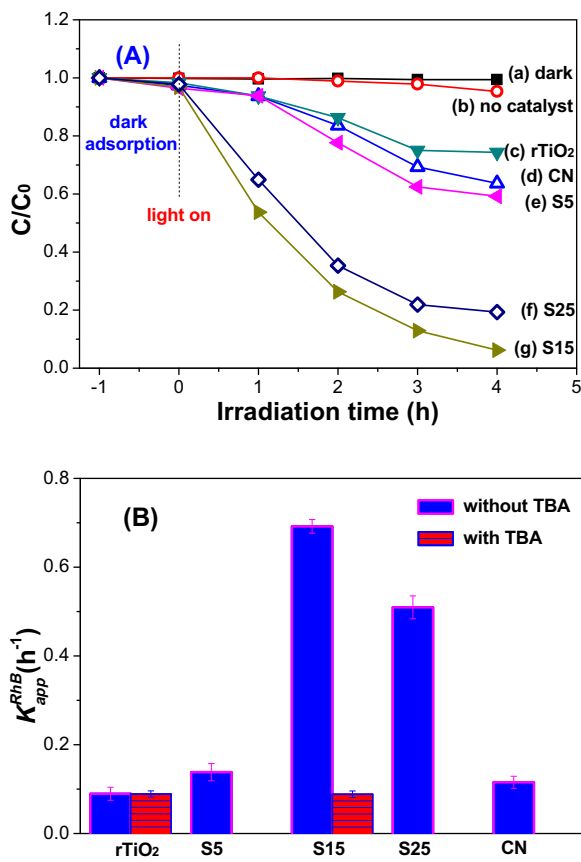


Fig. 8. Photocatalytic degradation profiles of RhB (A) and comparison of the corresponding rate constants (B).

3.7. Photocatalytic degradation of RhB

On the basis of the above results, we evaluated the visible-light-driven photocatalytic performance of as-obtained samples by utilizing RhB dye as a target contaminant of dye wastewater. Before running the photocatalytic reaction, adsorption-desorption tests were conducted on the photocatalysts. It was found that the adsorption-desorption behavior can reach an equilibrium after adsorption for 1 h. From Fig. 8A, it can be seen that both light and photocatalyst are necessary for efficient decomposition of RhB. The degradation profiles of RhB obey pseudo-first-order kinetics model, and comparison of the photocatalytic activity of the photocatalyst was shown in Fig. 8B. It can be seen that both rTiO₂ and CN showed poor reactivity with rate constants of only 0.089 h^{-1} and 0.12 h^{-1} , respectively. However, after modification of rTiO₂ with CN QDs, the photocatalytic activity of rTiO₂ was greatly enhanced, and S15 sample possesses the highest reactivity among all the hybrids. The degradation rate constant using S15 as photocatalyst is 0.69 h^{-1} , which is 7.8 and 6.0 times higher than pristine rTiO₂ and CN samples, respectively. This finding is reasonable, because hybridization of rTiO₂ with CN QDs can cause efficient separation of photo-generated electron-hole pairs, enhancing the photocatalytic activity. However, too many CN QDs could also cover the surface of rTiO₂, reducing the density of active sites, creating a light screening effect on the rTiO₂ surface, and thus decreasing the photocatalytic activity. As a result, the suitable loading content of CN QDs is a primary prerequisite for optimizing the photocatalytic reaction.

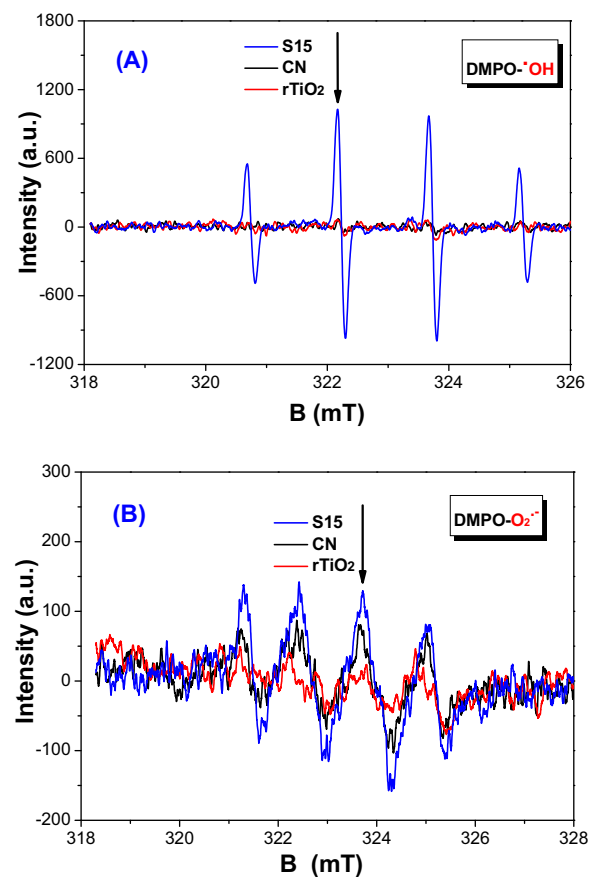


Fig. 9. DMPO spin-trapping ESR spectra under visible light irradiation ($\lambda > 420 \text{ nm}$) for 15 min in aqueous solutions (A) and ethanol solutions (B), respectively.

3.8. Active species for photocatalytic degradation of RhB

Reactive species, such as super oxygen ions ($O_2^{\bullet-}$), electron holes (h^+), and hydroxyl radicals ($\bullet\text{OH}$), have been identified to perform vital functions in the photocatalytic degradation process. To study the degradation mechanism of RhB, we conducted trapping experiments using TEA (scavenger for holes), TBA (scavenger for $\bullet\text{OH}$ radicals) and N_2 gas flow (scavenger for $O_2^{\bullet-}$) as scavengers to identify the main active species.

As shown in Fig. S2, the characteristic absorption peak variation of RhB at 554 nm was pursued to monitor the photocatalytic degradation main active group at different time intervals of visible-light exposure. In the case of rTiO₂, the maximum absorption of RhB suspension in the presence of rTiO₂ (554 nm) slightly shifted toward a lower wavelength (547 nm) after irradiation for 4 h. The addition of TBA into rTiO₂ suspensions did not affect the peak position of RhB filtrate, indicating that $\bullet\text{OH}$ was not the main active radical in naked rTiO₂. By contrast, no considerable change in the positions of maximum absorption of RhB was observed after the introduction of TEA or N_2 gas flow, indicating that the TEA and N_2 gas flow perform an inhibitory function in the photocatalytic process. In other words, h^+ and $O_2^{\bullet-}$ are the main active radicals in photocatalysis. For the S15 hybrid system, a strong shift from 554 nm to 524 nm occurred after 4 h of irradiation, whereas the maximum absorption position and intensity of RhB remain almost unchanged when TEA and TBA were added. Therefore, as mainly active species, h^+ and $\bullet\text{OH}$ can be responsible for the improved photocatalytic activity. Meanwhile, as seen from Fig. 8B, when then introduction of TBA, for rTiO₂, the apparent rate constant (k value) almost remains unchanged, while for S15, k value sharply decreased from 0.69 h^{-1}

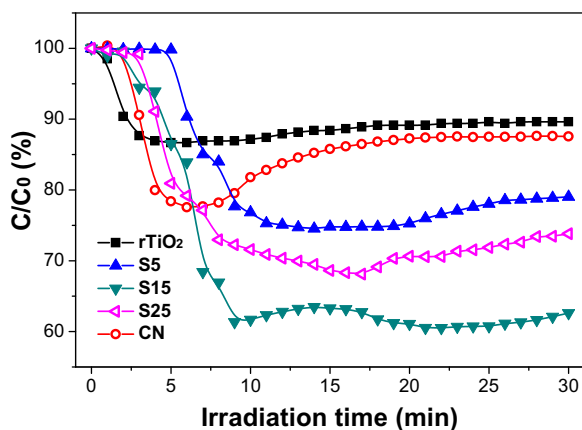


Fig. 10. Comparison of the photocatalytic NO removal efficiencies in a single-pass flow of air over different photocatalysts under visible-light irradiation.

to 0.088 h^{-1} , decreased 87%, further confirming that $\cdot\text{OH}$ radicals play important roles on the degradation of RhB over CN-QDs-rTiO₂ photocatalyst.

3.9. DMPO spin-trapping ESR spectrum

We used DMPO spin-trapping ESR spectrum to study the effect of CN QDs modification on the formation of $\cdot\text{OH}$ and $\text{O}_2^{\bullet-}$ radicals for rTiO₂. It can be seen from Fig. 9A that negligible signals for $\cdot\text{OH}$ radicals can be detected for rTiO₂ and CN samples. Although photo-generated holes of rutile TiO₂ have higher oxidation power than $\cdot\text{OH}$ radicals, the failure detection of $\cdot\text{OH}$ radicals in rutile TiO₂ suspensions has been ascribed to the quick recombination of photo-generated electron-hole pairs [42]. The potential of the photo-generated hole in the VB of g-C₃N₄ is not higher enough to oxidize H₂O to produce $\cdot\text{OH}$ radicals ($E_{\text{o}(-\text{OH}/\cdot\text{OH})} = 2.4 \text{ V}$). Therefore, it is understandable the failure detection of $\cdot\text{OH}$ radicals in rTiO₂ and CN suspensions under visible light irradiation.

However, the signal of $\cdot\text{OH}$ radicals was greatly enhanced for S15 sample, and the signal of $\text{O}_2^{\bullet-}$ radicals was also improved simultaneously (Fig. 9B). This indicates the increased photocatalytic activity of CN QDs modified rTiO₂, consistent with the result in photocatalytic degradation of RhB (Fig. 8).

According to the characterization results of DRS (Fig. 5A) and UPS (Fig. S4), the VB and CB edges of CN were measured to be +1.15 and -1.24 V versus NHE, while the VB and CB edges for rTiO₂ were +2.74 and -0.23 V versus NHE. Since the VB potential of CN is lower than that of the normal potential of the OH⁻/ $\cdot\text{OH}$ (+2.4 V versus NHE) [45], it can be predicted that the photo-generated holes on the surface of g-C₃N₄ cannot react with OH⁻/H₂O to form $\cdot\text{OH}$ radical. This has been confirmed by ESR (Fig. 9) and radicals quenching experiments (Figs. 8B and S2). The traditional heterojunction was unlikely to take place, and therefore a Z-scheme mechanism was proposed. As shown in Scheme 1, under visible light irradiation, the photo-induced electrons on the CB of rTiO₂ are moved to the VB of CN QDs, which can be further excited to the CB of CN QDs, leaving behind the photo-generated holes in the VB of rTiO₂. The electrons in the CB of CN QDs can be easily captured by adsorbed oxygen to form $\text{O}_2^{\bullet-}$, while holes in the VB of rTiO₂ can react with OH⁻/H₂O to generate $\cdot\text{OH}$ radicals. Both $\text{O}_2^{\bullet-}$ and $\cdot\text{OH}$ radicals are important active oxygen species for oxidation of organic pollutants.

3.10. Photocatalytic oxidation of NO

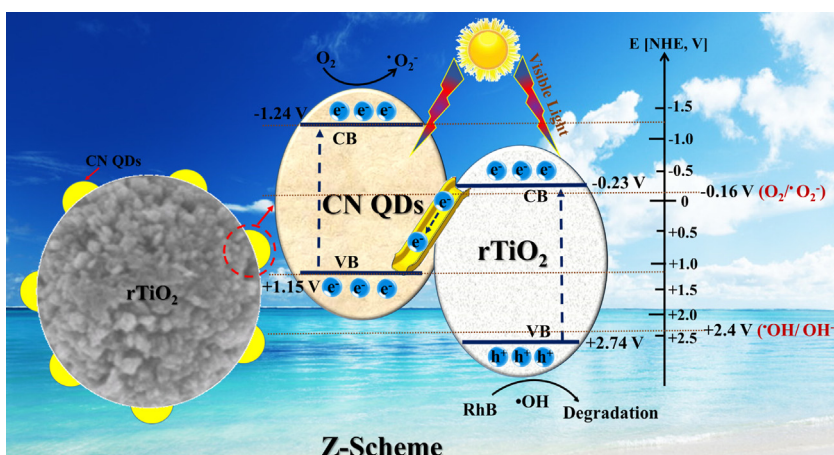
We further investigated the photocatalytic performance of the as-obtained samples by evaluating the photocatalytic removal of NO under visible-light irradiation. As shown in Fig. 10, pure rTiO₂ and CN exhibited relatively low photocatalytic efficiencies of 10.4 and 12.5%, respectively. After the introduction of only a small amount of CN QDs into rTiO₂, the photoactivity of CN QDs-rTiO₂ hybrids was markedly enhanced, especially for S15 composite with 37.4% removal efficiency of NO under visible-light illumination for 30 min, which is 3.6 and 3.0 times higher than pristine rTiO₂ and CN, respectively.

According to the study of Dong et al., both $\cdot\text{OH}$ and $\text{O}_2^{\bullet-}$ radicals are involved in the photocatalytic oxidation of NO [44]. The trend for photocatalytic removal of NO is in good agreement with the result of the photocatalytic degradation of RhB solution, corroborating that the optimal molar ratio of CN QDs-rTiO₂ hybrid (15 at.%) can provide guidance for an enhanced photocatalytic performance for both organic pollutant degradation and air purification, as shown in Scheme 1.

3.11. Possible mechanism

Based on the earlier discussion and results, in case of CN QDs-rTiO₂ system, through the trapping active species experiments, confirming the presence of h^+ and $\cdot\text{OH}$ radicals in the overall reaction period and acting as main reactive species for excellent photocatalytic performance.

According to the characterization results of DRS (Fig. 5A) and UPS (Fig. S4), the VB and CB edges of CN were measured to be +1.15 and -1.24 V versus NHE, while the VB and CB edges for rTiO₂ were +2.74 and -0.23 V versus NHE. Since the VB potential of CN is lower than that of the normal potential of the OH⁻/ $\cdot\text{OH}$ (+2.4 V versus NHE) [45], it can be predicted that the photo-generated holes on the surface of g-C₃N₄ cannot react with OH⁻/H₂O to form $\cdot\text{OH}$ radical. This has been confirmed by ESR (Fig. 9) and radicals quenching experiments (Figs. 8B and S2). The traditional heterojunction was unlikely to take place, and therefore a Z-scheme mechanism was proposed. As shown in Scheme 1, under visible light irradiation, the photo-induced electrons on the CB of rTiO₂ are moved to the VB of CN QDs, which can be further excited to the CB of CN QDs, leaving behind the photo-generated holes in the VB of rTiO₂. The electrons in the CB of CN QDs can be easily captured by adsorbed oxygen to form $\text{O}_2^{\bullet-}$, while holes in the VB of rTiO₂ can react with OH⁻/H₂O to generate $\cdot\text{OH}$ radicals. Both $\text{O}_2^{\bullet-}$ and $\cdot\text{OH}$ radicals are important active oxygen species for oxidation of organic pollutants.



Scheme 1. Photocatalytic degradation mechanism of CN QDs-rTiO₂ hybrid for RhB degradation and NO removal under visible-light irradiation.

and decomposition of nitrogen oxides. The coupling of CN QDs and rTiO₂ using this Z-scheme model not only facilitates the separation of photo-generated electrons and holes (PL in Fig. 5B, photocurrent and EIS in Fig. 6, and SPS in Fig. S3), but also increases the oxidation and reduction ability (ESR in Fig. 9), enhancing the photocatalytic activity (degradation of RhB in Fig. 8 and NO in Fig. 10).

4. Conclusion

In summary, CN QDs-rTiO₂ hybrid was successfully fabricated by a simple mixing-calcination approach. After modification of rTiO₂ with CN QDs, both the reactivity of visible-light-induced photodegradation of RhB and photooxidation of NO were significantly improved. The enhanced photocatalytic activity of QDs-rTiO₂ hybrid could be attributed to the synergistic effects of increased optical property and effective separation and transfer of photo-generated charges. •OH radicals quenching experiments and ESR radicals' detection support a Z-scheme degradation mechanism for CN QDs-rTiO₂ hybrids. This work makes the application of CN QDs-rTiO₂ composite possible both in wastewater treatment and air purification under sunlight irradiation.

Acknowledgements

This work was supported by National Program on Key Basic Research Project (2016YFA0203000) and Internal Research Grant (RG 11/2016–2017R), EdUHK, the Program for New Century Excellent Talents in University (NCET-12-0668) and National Natural Science Foundation of China (51672312 & 21373275). This work was also supported by the Croucher Foundation Visitorship for PRC Scholars 2015/16 in The Education University of Hong Kong.

Appendix A. Supplementary data

Supplementary data associated with this article can be found, in the online version, at <http://dx.doi.org/10.1016/j.apcatb.2016.09.055>.

References

- [1] A.J. Willian, V.J. Henry, *PNAS* 102 (2005) 15715–15720.
- [2] J.C. Swarbrick, U. Skyllberg, T.r. Karlsson, P. Glatzel, *Inorg. Chem.* 48 (2009) 10748–10756.
- [3] A. Fujishima, K. Honda, *Nature* 238 (1972) 37.
- [4] G.H. Dong, W.K. Ho, Y.H. Li, L.Z. Zhang, *Appl. Catal. B* 174 (2015) 477–485.
- [5] X.X. Xu, C. Randorn, P. Efstatou, J.T.S. Irvine, *Nature Mater.* 11 (2012) 595–598.
- [6] X.F. Wu, L.L. Wen, K.L. Lv, K.J. Deng, D.G. Tang, H.P. Ye, D.Y. Du, S.N. Liu, M. Li, *Appl. Surf. Sci.* 358 (2015) 130–136.
- [7] Z.F. Hu, Z.R. Shen, J.C. Yu, *Chem. Mater.* 28 (2016) 564–572.
- [8] Z.F. Hu, G. Liu, X.Q. Chen, Z.R. Shen, J.C. Yu, *Adv. Funct. Mater.* 26 (2016) 4445–4455.
- [9] J.W. Tang, J.R. Durrant, D.R. Klug, *J. Am. Chem. Soc.* 130 (2008) 13885–13891.
- [10] M.R. Hoffmann, S.T. Martin, W. Choi, D.W. Bahnemann, *Chem. Rev.* 95 (1995) 69–96.
- [11] A. Fujishima, X. Zhang, C. R. Chim. 9 (2006) 750–760.
- [12] A. Fujishima, X. Zhang, D.A. Tryk, *Int. J. Hydrogen Energy* 32 (2007) 2664–2672.
- [13] A.J. Frank, N. Kopidakis, J. van de Lagemaat, *Coordin. Chem. Rev.* 248 (2004) 1165–1179.
- [14] J.F. Lan, X.F. Wu, K.L. Lv, L.L. Si, K.J. Deng, *Chin. J. Catal.* 36 (2015) 2237–2243.
- [15] L.D. Li, J.Q. Yan, T. Wang, Z.J. Zhao, J. Zhang, J.L. Gong, N.J. Guan, *Nat. Commun.* 6 (2015).
- [16] F. Dong, Y.H. Li, Z.Y. Wang, W.K. Ho, *Appl. Surf. Sci.* 358 (2015) 393–403.
- [17] S. Fang, K.L. Lv, Q. Li, H. Ye, D. Du, M. Li, *Appl. Surf. Sci.* 358 (2015) 336–342.
- [18] S. Fang, Y. Xia, K.L. Lv, Q. Li, J. Sun, M. Li, *Appl. Catal. B* 185 (2016) 225–232.
- [19] F. Dong, Z. Zhao, T. Xiong, Z. Ni, W. Zhang, Y. Sun, W.K. Ho, *ACS Appl. Mater. Interfaces* 5 (2013) 11392–11401.
- [20] Q. Li, X. Li, S. Wageh, A. Al-Ghamdi, J. Yu, *Adv. Energy Mater.* 5 (2015).
- [21] Y.P. Zang, L.P. Li, Y.S. Xu, Y. Zuo, G.S. Li, *J. Mater. Chem. A* 2 (2014) 15774–15780.
- [22] C. Miranda, H. Mansilla, J. Yáñez, S. Obregón, G. Colón, *J. Photochem. Photobiol. A* 253 (2013) 16–21.
- [23] J.G. Yu, S.H. Wang, J.X. Low, W. Xiao, *Phys. Chem. Chem. Phys.* 15 (2013) 16883–16890.
- [24] Z.A. Huang, Q. Sun, K.L. Lv, Z.H. Zhang, M. Li, B. Li, *Appl. Catal. B* 164 (2015) 420–427.
- [25] W.J. Wang, C.Y. Jimmy, Z.R. Shen, D.K.L. Chan, T. Gu, *Chem. Commun.* 50 (2014) 10148–10150.
- [26] G.S. Li, Z.C. Lian, W.C. Wang, D.Q. Zhang, H.X. Li, *Nano Energy* 19 (2016) 446–454.
- [27] T. An, J. Tang, Y. Zhang, Y. Quan, X. Gong, A.M. Al-Enizi, A.A. Elzatahry, L. Zhang, G. Zheng, *ACS Appl. Mater. Interfaces* 8 (2016) 12772–12779.
- [28] J. Li, M. Zhang, Q.Y. Li, J.J. Yang, *Appl. Surf. Sci.* (2016), <http://dx.doi.org/10.1016/j.apsusc.2016.06.145>.
- [29] G.Y. Li, X. Nie, J.Y. Chen, Q. Jiang, T.C. An, P.K. Wong, H.M. Zhang, H.J. Zhao, H. Yamashita, *Water Res.* 86 (2015) 17–24.
- [30] J.X. Wang, J. Huang, H.L. Xie, A.L. Qu, *Int. J. Hydrogen Energy* 39 (2014) 6354–6363.
- [31] D.T. Zhou, Z. Chen, Q. Yang, X.P. Dong, J.J. Zhang, L.S. Qin, *Solar Energy Mater. Sol. Cell.* 157 (2016) 399–405.
- [32] S.C. Yan, Z.S. Li, Z.G. Zou, *Langmuir* 26 (2010) 3894–3901.
- [33] S.C. Yan, Z.S. Li, Z.G. Zou, *Langmuir* 25 (2009) 10397–10401.
- [34] K. Lv, C.S. Lu, *Chem. Eng. Technol.* 31 (2008) 1272–1276.
- [35] G. Liao, S. Chen, X. Quan, H. Yu, H. Zhao, J. Mater. Chem. 22 (2012) 2721–2726.
- [36] J.W. Zhou, M. Zhang, Y.F. Zhu, *Phys. Chem. Chem. Phys.* 17 (2015) 3647–3652.
- [37] X.Y. Pan, X.X. Chen, Z.G. Yi, *ACS Appl. Mater. Interfaces* 8 (2016) 10104–10108.
- [38] L. Ge, C.C. Han, J. Liu, Y.F. Li, *Appl. Catal. A* 409–410 (2011) 215–222.
- [39] J.G. Yu, J.C. Yu, *Chin. J. Chem.* 21 (2003) 994–997.
- [40] Y.Y. Kang, Y.Q. Yang, L.C. Yin, X.D. Kang, L.Z. Wang, G. Liu, H.M. Cheng, *Adv. Mater.* 28 (2016) 6471–6477.
- [41] J.G. Yu, W.G. Wang, B. Cheng, *Chem. Asian J.* 5 (2010) 2499–2506.
- [42] K.L. Lv, X.F. Li, K.J. Deng, J. Sun, X.H. Li, M. Li, *Appl. Catal. B* 95 (2010) 383–392.
- [43] L.W. Zhang, H.B. Fu, Y.F. Zhu, *Adv. Funct. Mater.* 18 (2008) 2180–2189.
- [44] F. Dong, Z.W. Zhao, Y.J. Sun, Y.X. Zhang, S. Yan, Z.B. Wu, *Environ. Sci. Technol.* 49 (2015) 12432–12440.
- [45] W. Wang, B. Cheng, J. Yu, G. Liu, W. Fan, *Chem. Asian J.* 7 (2012) 1902–1908.